Monthly Notices
of the
ROYAL ASTRONOMICAL SOCIETY

Mon. Not. R. Astron. Soc. **410,** 2003–2015 (2011) doi:10.1111/j.1365-2966.2010.17578.x

Generalized Schwarzschild's method

Mir Abbas Jalali[1,2⋆] and Scott Tremaine[2⋆]

[1] *Sharif University of Technology, Postal Code 14588-89694, Azadi Avenue, Tehran, Iran*
[2] *School of Natural Sciences, Institute for Advanced Study, Einstein Drive, Princeton, NJ 08540, USA*

Accepted 2010 August 22. Received 2010 August 20; in original form 2010 July 19

ABSTRACT

We describe a new finite element method (FEM) to construct continuous equilibrium distribution functions (DFs) of stellar systems. The method is a generalization of Schwarzschild's orbit superposition method from the space of discrete functions to continuous ones. In contrast to Schwarzschild's method, FEM produces a continuous DF and satisfies the intra-element continuity and Jeans equations. The method employs two finite element meshes, one in configuration space and one in action space. The DF is represented by its values at the nodes of the action-space mesh and by interpolating functions inside the elements. The Galerkin projection of all equations that involve the DF leads to a linear system of equations, which can be solved for the nodal values of the DF using linear or quadratic programming, or other optimization methods. We illustrate the superior performance of FEM by constructing ergodic and anisotropic equilibrium DFs for spherical stellar systems (Hernquist models). We also show that explicitly constraining the DF by the Jeans equations leads to smoother and/or more accurate solutions with both Schwarzschild's method and FEM.

Key words: methods: numerical – galaxies: elliptical and lenticular, cD – galaxies: kinematics and dynamics – galaxies: structure.

1 INTRODUCTION

For over three decades, Schwarzschild's (1979) orbit superposition method has been one of the most important numerical tools for modelling the equilibrium states of spherical (Richstone & Tremaine 1984), axisymmetric (Thomas et al. 2004) and triaxial galaxies (van den Bosch et al. 2008 and references therein). Schwarzschild's method constructs discrete phase-space distribution functions (DF) and works even if the gravitational potential supports chaotic orbits (e.g. Capuzzo-Dolcetta et al. 2007). Observational constraints can also be incorporated, in particular on the surface brightness or the line-of-sight velocity distributions. Schwarzschild's basic assumptions were: (i) the amount of mass contributed by an orbit to a cell/element in the configuration space is proportional to the fraction of time spent by that orbit inside the element; (ii) the matter density and velocity distribution inside each element are constant; (iii) the DF is non-zero only on a subset of phase space with measure zero (except perhaps in some cases where the potential admits large-scale chaos). In particular, if all orbits are regular the DF is discrete, i.e. non-zero only at a finite set of positions in action space.

Despite its central role in modelling galaxies, Schwarzschild's method has several shortcomings. (i) There is no mathematical proof that increasing the number of elements and orbits in this scheme will guarantee the convergence of the coarse-grained DF to a smooth function. (ii) In practice, Schwarzschild models often converge rather slowly, in part because of the inverse square-root singularity in the density contributed by an orbit near a turning point. (iii) Working with discrete DFs is not ideal if we require their derivatives for linear stability analysis, or use them to set initial conditions for N-body simulations.

The majority of these limitations can be removed if one extends the method from the space of discrete functions to a more general continuous class. This is a problem in galactic dynamics whose solution is overdue, and we aim to solve it using a modified finite element method (FEM). Essentially, we replace the finite set of delta functions in action space that represent the DF in Schwarzschild's method by a piecewise continuous function; the FEM can also be generalized to construct differentiable DFs but we do not describe this extension in the present paper.

The mathematical principles of FEM are rather simple. Assume a general governing equation

$$\mathcal{A}[u(\boldsymbol{x},t)]=0 \tag{1}$$

for the physical quantity $u(\boldsymbol{x},t)$, with $\mathcal{A}$ being a partial integro-differential operator, and seek the solutions in terms of the coordinates $\boldsymbol{x}$ and the time t. An approximate solution of (1) may be expanded as the series

$$u(\boldsymbol{x},t)=\sum_{j=1}^{j_{\max}} u_j(t)\psi_j(\boldsymbol{x}), \tag{2}$$

⋆E-mail: mjalali@sharif.edu (MAJ); tremaine@ias.edu (ST)

where $\psi_j(\boldsymbol{x})$ constitute a complete set of basis functions that satisfy any given boundary conditions. Substituting (2) into (1), multiplying both sides of the resulting equation by $\psi_{j'}(\boldsymbol{x})$ and integrating over the $\boldsymbol{x}$ domain result in

$$\int \psi_{j'}(\boldsymbol{x})\mathcal{A}[u(\boldsymbol{x},t)]\mathrm{d}\boldsymbol{x}=0, \quad j'=1,2,\ldots,j_{\max}. \tag{3}$$

This is called the weighted residual form, weak form or Galerkin projection of the governing equation (1), from which one may compute the unknown functions $u_j(t)$. Here, the basic assumption is that if the equations (3) are satisfied for all j' then equation (1) is also satisfied to an adequate degree of approximation.

It is, however, a non-trivial and sometimes impossible task to find suitable basis functions that (i) satisfy all boundary conditions, (ii) make a complete set, (iii) do not contribute noise when the solution is changing rapidly. Moreover, the integration over the spatial variables is expensive if the domain of each basis function is the entire $\boldsymbol{x}$-space. One can overcome these difficulties by dividing the $\boldsymbol{x}$-space into *N finite elements*. The union of elements, each of volume V_n, is the entire $\boldsymbol{x}$ domain. Each element contains N_d nodes on its boundaries or in its interior. The function u is approximated inside the nth element as a weighted sum of smooth shape functions $\hat{\psi}_{nj}(\boldsymbol{x})$; these are defined only within element n and are zero at all nodes except node j of bin n, where they are unity. The weights u_{nj} are time-dependent and are chosen to fit the unknown value of u at the nodes. The determining equations of the weights are

$$\begin{aligned}&\int_{V_n}\hat{\psi}_{n'j'}(\boldsymbol{x})\mathcal{A}[u(\boldsymbol{x},t)]\mathrm{d}\boldsymbol{x}\\&=\int_{V_n}\hat{\psi}_{n'j'}(\boldsymbol{x})\mathcal{A}\left[\sum_{n,j}u_{nj}(t)\hat{\psi}_{nj}(\boldsymbol{x})\right]\mathrm{d}\boldsymbol{x}=0,\\&\qquad n'=1,2,\ldots,N,\quad j'=1,\ldots,N_\mathrm{d}.\end{aligned} \tag{4}$$

This procedure, which leaves us with a system of ordinary integro-differential equations for the weights $u_{jk}(t)$ (the nodal values of u), is called the FEM (Zienkiewicz, Taylor & Zhu 2005).

For example, when the operator $\mathcal{A}$ has the form $\mathcal{A}u=\partial u/\partial t+\mathcal{L}u$ with $\mathcal{L}(t)$ a linear operator, the weighted residual form takes a simple matricial form

$$\frac{\mathrm{d}}{\mathrm{d}t}\boldsymbol{u}(t)=\mathbf{A}(t)\cdot\boldsymbol{u}(t)+\boldsymbol{F}(t), \tag{5}$$

where the matrix $\mathbf{A}(t)$ is the projection of the operator $-\mathcal{L}$ and $\boldsymbol{F}(t)$ is a forcing vector. The vector $\boldsymbol{u}(t)$ contains nodal values of $u(\boldsymbol{x},t)$. Therefore, the combination of finite elements and Galerkin projection reduces an infinite-dimensional partial differential equation to a finite-dimensional system.

A formulation of FEM for stellar systems was presented in Jalali (2010), where the perturbed collisionless Boltzmann equation (CBE) was reduced to a form like (5) and solved over a range of finite ring elements in the configuration space. That analysis, however, cannot be directly used to construct equilibrium DFs because they are not unique: according to the Jeans theorem, any DF f that depends on phase space coordinates only through the integrals of motion $\boldsymbol{I}$ is an equilibrium solution of the CBE. Consequently, the local variation of f in the $\boldsymbol{I}$-space is free. This implies non-uniqueness, and f can admit discrete, piece-wise continuous, continuous and differentiable solutions.

In this paper, we develop a general method to build numerical DFs that exhibit nice properties of differentiability within each element and continuity across elements. After defining the problem in Section 1.1, in Section 2 we discuss finite elements, interpolation functions, and their properties in both the configuration and action spaces. In Section 3, we obtain the Galerkin projections of velocity moments, and the continuity and Jeans equations. Schwarzschild's method is derived as a special case of FEM in Section 4, and finite element models of spherical systems are discussed in Section 5. We apply the FEM to the spherical Hernquist model in Section 6 and Section 7 contains a discussion of our results. The reader who would like to see a direct comparison of the two methods can turn to Fig. 3, which shows the ergodic, spherical, Hernquist model: the errors in the FEM model on the left are about five times smaller than the errors in the Schwarzschild models on the right.

1.1 Equilibrium stellar systems

The DF of a collisionless system in dynamical equilibrium depends on the position $\boldsymbol{x}=(x_1,x_2,x_3)$ and the velocity $\boldsymbol{v}=(v_1,v_2,v_3)$ vectors only through the integrals of motion.

Integrable systems. The Hamilton–Jacobi equation is separable in spherical systems, razor-thin axisymmetric discs and triaxial systems in which the potential is of Stäckel form. Orbits in these systems are regular, and can be represented using a suitable action vector $\boldsymbol{J}=(J_1,J_2,J_3)$ and its associated angle variables $\boldsymbol{w}=(w_1,w_2,w_3)$. The Hamiltonian function $\mathcal{H}$ depends only on the action vector and the evolution of the angle variables is linear in time:

$$\boldsymbol{w}(t)=\boldsymbol{\Omega}t+\boldsymbol{w}(0),\quad \boldsymbol{\Omega}(\boldsymbol{J})=\frac{\partial\mathcal{H}}{\partial\boldsymbol{J}}, \tag{6}$$

where $\boldsymbol{\Omega}=(\Omega_1,\Omega_2,\Omega_3)$ is the vector of orbital frequencies. The actions are isolating integrals of motion, so any DF of the form $f(\boldsymbol{J})$ defines a possible equilibrium stellar system. For separable systems, the actions can be computed by quadratures. In this study, we focus on building equilibrium models of stellar systems with integrable potentials.

Non-integrable systems. Generic axisymmetric or triaxial potentials are not integrable. There are surviving invariant tori of regular orbits (cf. KAM theory) but these are separated by chaotic layers. If the chaotic layers are narrow (the potential is 'nearly integrable') the DF may be assumed to be zero in the chaotic phase subspace and written as a function of the actions in the regular phase subspace. However, the actions must then be calculated either using canonical perturbation theory or by generating a frequency map of the system (Laskar 1990; Hunter 2002; Binney & Tremaine 2008).

A simpler and more powerful approach, which can be used even if the potential is far from integrability, is to express the integrals of motion in terms of initial conditions of orbits (Schwarzschild 1979). Thus, let $[\boldsymbol{x}_0(\boldsymbol{x},\boldsymbol{v}),\boldsymbol{v}_0(\boldsymbol{x},\boldsymbol{v})]$ be the position and velocity of the trajectory through $(\boldsymbol{x},\boldsymbol{v})$ on some global surface of section $\mathcal{D}$ through which all orbits must pass (e.g. a symmetry plane of a triaxial potential). Then, any DF of the form $f(\boldsymbol{x}_0,\boldsymbol{v}_0)$ defines an equilibrium stellar system.

1.1.1 Moments of the DF

A collisionless system with a given density function $\rho(\boldsymbol{x})$ is a possible equilibrium if one can find a DF $f(\boldsymbol{J})\geq 0$ so that

$$\rho(\boldsymbol{x})=\int f(\boldsymbol{J})\mathrm{d}\boldsymbol{v}. \tag{7}$$

We shall also sometimes use the first- and second-order velocity moments:

$$u^i(\boldsymbol{x})\equiv\rho\,\langle v_i\rangle(\boldsymbol{x})=\int v_i f(\boldsymbol{J})\mathrm{d}\boldsymbol{v}, \tag{8}$$

$$\tau^{ij}(\boldsymbol{x}) \equiv \rho\langle v_i v_j\rangle(\boldsymbol{x}) = \int v_i v_j f(\boldsymbol{J})\mathrm{d}\boldsymbol{v}. \tag{9}$$

In an equilibrium system these are related by the steady-state continuity equation

$$\sum_{i=1}^{3} \frac{\partial u^i}{\partial x_i} = 0, \tag{10}$$

and Jeans equations

$$\sum_{j=1}^{3} \frac{\partial \tau^{ij}}{\partial x_j} = -\rho \frac{\partial \Phi}{\partial x_i}, \quad i = 1, 2, 3, \tag{11}$$

with $\Phi(\boldsymbol{x})$ being the potential. In systems with spherical symmetry only the radial and tangential velocity dispersions matter and three Jeans equations reduce to one.

We shall argue below that including constraints based on the continuity and Jeans equations can significantly improve the accuracy of both Schwarzschild and FEM models of stellar systems.

2 FINITE ELEMENTS IN CONFIGURATION AND ACTION SPACE

We assume that the configuration space has been split into N elements, each of N_d nodes, and that the density $\rho(\boldsymbol{x})$ is known at the nodal points. Inside each element, the density function can be approximated by suitable interpolation (shape) functions. Denoting $\rho_n(\boldsymbol{x})$ as the functional form of the density inside the nth element, one may write

$$\rho(\boldsymbol{x}) = \sum_{n=1}^{N} H_n(\boldsymbol{x})\rho_n(\boldsymbol{x}), \quad \rho_n(\boldsymbol{x}) = \sum_{k=1}^{N_\mathrm{d}} g_{k,n}(\boldsymbol{x})\rho_{k,n}. \tag{12}$$

The density at the kth node of the nth element has been indexed by the pair (k, n). The function $H_n(\boldsymbol{x})$ is unity inside the nth element in the $\boldsymbol{x}$-space and zero outside. The interpolation functions $g_{j,n}(\boldsymbol{x})$ have the following properties:

$$g_{j,n}(\boldsymbol{x}_{kn}) = \delta_{jk}, \quad j, k = 1, 2, \ldots, N_\mathrm{d}, \tag{13}$$

where δ_{jk} is the Kronecker delta, and $\boldsymbol{x}_{kn}$ is the position vector of the kth node of the nth element. Fig. 1 shows some elementary one-, two- and three-dimensional elements. The rectangular and brick elements can be distorted to obtain the so-called mapped elements (Zienkiewicz et al. 2005), which help to reconstruct complex morphologies in curvilinear coordinates. For instance, elements confined between confocal ellipsoids and hyperboloids can better describe elliptical galaxy models that may have potentials close to the Stäckel form. Thin rings and spherical shells are the most efficient elements for axisymmetric discs and spherical systems, respectively.

Using the superscript 'T' to transpose a vector/matrix, we define the row vector

$$\boldsymbol{g}_n(\boldsymbol{x}) = [\, g_{1,n}(\boldsymbol{x}) \quad g_{2,n}(\boldsymbol{x}) \quad \cdots \quad g_{N_\mathrm{d},n}(\boldsymbol{x})\,], \tag{14}$$

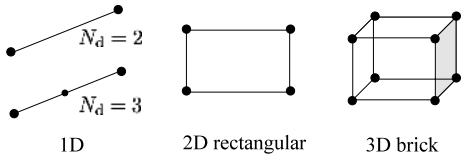

Figure 1. Elementary finite elements. The degree of interpolating polynomial increases by adding interior nodes, which can lie on the edges, sides or even inside elements.

and the column vector

$$\boldsymbol{b}_n = [\, \rho_{1,n} \quad \rho_{2,n} \quad \cdots \quad \rho_{N_\mathrm{d},n}\,]^\mathrm{T}, \tag{15}$$

and rewrite the components of $\rho_n(\boldsymbol{x})$ in the following compact form

$$\rho_n = \boldsymbol{g}_n \cdot \boldsymbol{b}_n. \tag{16}$$

Here, a dot denotes matrix/vector multiplication. The above procedure can be readily applied to higher order velocity moments. In particular, we obtain

$$u_n^i = \boldsymbol{g}_n \cdot \boldsymbol{c}_n^i, \quad \tau_n^{ij} = \boldsymbol{g}_n \cdot \boldsymbol{d}_n^{ij}, \tag{17}$$

where the column vectors $\boldsymbol{c}_n^i$ and $\boldsymbol{d}_n^{ij}$ contain, respectively, the nodal values of u^i and τ^{ij} inside the nth element.

To construct a DF $f(\boldsymbol{J})$, we divide the action space into M finite elements, each of M_d nodes, and write

$$f(\boldsymbol{J}) = \sum_{m=1}^{M} H_m(\boldsymbol{J}) f_m(\boldsymbol{J}), \quad f_m(\boldsymbol{J}) = \sum_{j=1}^{M_\mathrm{d}} h_{j,m}(\boldsymbol{J}) f_{j,m}, \tag{18}$$

where the interpolation functions $h_{j,m}(\boldsymbol{J})$ satisfy the condition

$$h_{j,m}(\boldsymbol{J}_{km}) = \delta_{jk}, \quad j, k = 1, 2, \ldots, M_\mathrm{d}, \tag{19}$$

at the action vector $\boldsymbol{J}_{km}$ associated with the kth node of the mth element in action space. The union of the domains of $h_{j,m}$ covers the action space. The components of f_m can be rewritten in the form

$$\begin{aligned} f_m &= \boldsymbol{h}_m \cdot \boldsymbol{p}_m \\ \boldsymbol{h}_m(\boldsymbol{J}) &= [\, h_{1,m}(\boldsymbol{J}) \quad h_{2,m}(\boldsymbol{J}) \quad \cdots \quad h_{M_\mathrm{d},m}(\boldsymbol{J})\,], \\ \boldsymbol{p}_m &= [\, f_{1,m} \quad f_{2,m} \quad \cdots \quad f_{M_\mathrm{d},m}\,]^\mathrm{T}, \end{aligned} \tag{20}$$

analogous to equations (14)–(16).

In this study, we use interpolation functions of C_0 class in both the $\boldsymbol{x}$ and $\boldsymbol{J}$ spaces. The use of C_0 functions implies that all physical quantities are smooth (continuous and differentiable) inside each element and along its boundary lines. In the direction perpendicular to the boundary lines and at the nodes, the DF, density and higher-order velocity moments will only be continuous. For example, consider the simplest one-dimensional set of C_0 elements: element n has boundaries at x_n and $x_{n+1} > x_n$ and has two nodes, with node 1 at the smaller boundary x_n and node 2 at the larger. The continuity of $\rho(x)$ at $x = x_{n+1}$ implies $\rho_n(x_{n+1}) = \rho_{n+1}(x_{n+1})$. Using (13), this condition reduces to

$$b_{2,n} = b_{1,(n+1)}. \tag{21}$$

The first derivative of $\rho_n(x)$ with respect to x exists inside element n and is given by

$$\frac{\partial \rho_n}{\partial x} = b_{1,n}\frac{\partial g_{1,n}}{\partial x} + b_{2,n}\frac{\partial g_{2,n}}{\partial x}, \tag{22}$$

but the differentiability condition at the nodes of elements is not necessarily satisfied, i.e.

$$\left[\frac{\partial \rho_n}{\partial x}\right]_{x=x_{n+1}} \neq \left[\frac{\partial \rho_{n+1}}{\partial x}\right]_{x=x_{n+1}}. \tag{23}$$

One can resolve this problem by applying C_1 finite elements. The application of C_1 elements requires larger vectors of nodal quantities (which should now include partial derivatives), and thus larger element matrices. In this paper we restrict ourselves to C_0 elements; however, we note that C_1 elements provide smoother solutions (at the cost of larger matrices and greater analytic complexity), and are likely to be useful when the partial derivatives of $f(\boldsymbol{J})$ are also needed (e.g. in linear stability analyses).

3 GALERKIN WEIGHTING OF GOVERNING EQUATIONS

This section implements a Bubnov–Galerkin procedure (Zienkiewicz et al. 2005) to satisfy the governing equations of physical quantities (dependent variables) over individual elements in a weighted residual sense. As a result, independent variables are eliminated from equations, leaving a system of algebraic equations between nodal values of DF, density and velocity moments. The formulation is done in Cartesian coordinates, and it should be modified for non-Cartesian ones (see Section 5 for spherical systems).

3.1 Density and velocity moments

Inside the nth element in the configuration space, equation (7) reduces to

$$H_n(\boldsymbol{x})\rho_n(\boldsymbol{x}) = \int H_n(\boldsymbol{x}) f(\boldsymbol{J}) \mathrm{d}\boldsymbol{v}; \tag{24}$$

the presence of $H_n(\boldsymbol{x})$ on the right side ensures that the integration is carried out over a phase subspace whose particles visit the nth element and contribute to the density and velocity dispersion of that element. By substituting from (16) and (18) into (24) we obtain

$$H_n(\boldsymbol{x})\boldsymbol{g}_n(\boldsymbol{x}) \cdot \boldsymbol{b}_n = \sum_{m=1}^{M} H_m(\boldsymbol{J}) \int H_n(\boldsymbol{x}) \boldsymbol{h}_m(\boldsymbol{J}) \cdot \boldsymbol{p}_m \mathrm{d}\boldsymbol{v}. \tag{25}$$

Denoting $\otimes$ as the dyadic product, we operate with $\mathrm{d}\boldsymbol{x}\boldsymbol{g}_n(\boldsymbol{x})\otimes$ on equation (25), and integrate the result over the $\boldsymbol{x}$-domain to get

$$\mathbf{G}_n \cdot \boldsymbol{b}_n = \sum_{m=1}^{M} \iint \mathrm{d}\boldsymbol{x}\mathrm{d}\boldsymbol{v} H_m(\boldsymbol{J}) \times [H_n(\boldsymbol{x})\boldsymbol{g}_n(\boldsymbol{x}) \otimes \boldsymbol{h}_m(\boldsymbol{J})] \cdot \boldsymbol{p}_m, \tag{26}$$

with

$$\mathbf{G}_n = \int H_n(\boldsymbol{x})[\boldsymbol{g}_n(\boldsymbol{x}) \otimes \boldsymbol{g}_n(\boldsymbol{x})]\mathrm{d}\boldsymbol{x} \tag{27}$$

being an $N_\mathrm{d} \times N_\mathrm{d}$ constant matrix. The function $H_n(\boldsymbol{x})$ in the integrand of (27) restricts the domain of integration to the region occupied by the nth element. The integral in $\mathbf{G}_n$ can be done analytically should one use interpolation functions of polynomial type.

The transformation $(\boldsymbol{x}, \boldsymbol{v}) \rightarrow (\boldsymbol{w}, \boldsymbol{J})$ is canonical and so the infinitesimal phase-space volume $\mathrm{d}\boldsymbol{x}\mathrm{d}\boldsymbol{v}$ can be replaced by $\mathrm{d}\boldsymbol{w}\mathrm{d}\boldsymbol{J}$. Furthermore, the vectorial function $H_n(\boldsymbol{x})\boldsymbol{g}_n(\boldsymbol{x})$ can be expressed in terms of angle-action variables (Jalali 2010):

$$H_n(\boldsymbol{x})\boldsymbol{g}_n(\boldsymbol{x}) = \sum_{\boldsymbol{k}} \tilde{\boldsymbol{g}}_{\boldsymbol{k}}(n, \boldsymbol{J}) e^{\mathrm{i}\boldsymbol{k}\cdot\boldsymbol{w}}, \tag{28}$$

with $\tilde{\boldsymbol{g}}^*_{\boldsymbol{k}} = \tilde{\boldsymbol{g}}_{-\boldsymbol{k}}$. Here, the asterisk stands for complex conjugation, $\boldsymbol{k}$ is a three-vector of integers and $\mathrm{i} = \sqrt{-1}$. The row vector $\tilde{\boldsymbol{g}}_{\boldsymbol{k}}$ has the same dimension as $\boldsymbol{g}_n$ and it is calculated from

$$\tilde{\boldsymbol{g}}_{\boldsymbol{k}} = \frac{1}{(2\pi)^3} \int H_n(\boldsymbol{x})\boldsymbol{g}_n(\boldsymbol{x}) e^{-\mathrm{i}\boldsymbol{k}\cdot\boldsymbol{w}} \mathrm{d}\boldsymbol{w}. \tag{29}$$

When a test particle with the action vector $\boldsymbol{J}$ is inside the nth element in the configuration space, the function $H_n(\boldsymbol{x})$ is unity and that particle contributes to $\tilde{\boldsymbol{g}}_{\boldsymbol{k}}$. In other situations, the integrand of (29) will vanish.

Using (28), equation (26) is transformed to

$$\boldsymbol{b}_n = \sum_{m=1}^{M} \sum_{\boldsymbol{k}} \iint \mathrm{d}\boldsymbol{w}\mathrm{d}\boldsymbol{J} H_m(\boldsymbol{J}) e^{\mathrm{i}\boldsymbol{k}\cdot\boldsymbol{w}} \times \mathbf{G}_n^{-1} \cdot [\tilde{\boldsymbol{g}}_{\boldsymbol{k}}(n, \boldsymbol{J}) \otimes \boldsymbol{h}_m(\boldsymbol{J})] \cdot \boldsymbol{p}_m. \tag{30}$$

It is obvious that only the term with $\boldsymbol{k} = (0, 0, 0) \equiv \boldsymbol{0}$ contributes to the integral over the $\boldsymbol{w}$-space and equation (30) reads as

$$\boldsymbol{b}_n = \sum_{m=1}^{M} \mathbf{F}_\mathrm{e}(n, m) \cdot \boldsymbol{p}_m, \quad n = 1, 2, \ldots, N, \tag{31}$$

with

$$\mathbf{F}_\mathrm{e}(n, m) = (2\pi)^3 \int \mathrm{d}\boldsymbol{J} H_m(\boldsymbol{J}) \mathbf{G}_n^{-1} \cdot [\tilde{\boldsymbol{g}}_{\boldsymbol{0}}(n, \boldsymbol{J}) \otimes \boldsymbol{h}_m(\boldsymbol{J})]. \tag{32}$$

We define

$$\tilde{\boldsymbol{g}}_{\boldsymbol{0}}(i, n, \boldsymbol{J}) = \frac{1}{(2\pi)^3} \int v_i H_n(\boldsymbol{x}) \boldsymbol{g}_n(\boldsymbol{x}) \mathrm{d}\boldsymbol{w}, \tag{33}$$

$$\tilde{\boldsymbol{g}}_{\boldsymbol{0}}(i, j, n, \boldsymbol{J}) = \frac{1}{(2\pi)^3} \int v_i v_j H_n(\boldsymbol{x}) \boldsymbol{g}_n(\boldsymbol{x}) \mathrm{d}\boldsymbol{w}, \tag{34}$$

and repeat the above procedure for the functions $H_n(\boldsymbol{x})u^i(\boldsymbol{x})$ and $H_n(\boldsymbol{x})\tau^{ij}(\boldsymbol{x})$ to obtain

$$\boldsymbol{c}^i_n = \sum_{m=1}^{M} \mathbf{U}_\mathrm{e}(i, n, m) \cdot \boldsymbol{p}_m, \quad \boldsymbol{d}^{ij}_n = \sum_{m=1}^{M} \mathbf{S}_\mathrm{e}(i, j, n, m) \cdot \boldsymbol{p}_m, \tag{35}$$

where

$$\mathbf{U}_\mathrm{e} = (2\pi)^3 \int \mathrm{d}\boldsymbol{J} H_m(\boldsymbol{J}) \mathbf{G}_n^{-1} \cdot [\tilde{\boldsymbol{g}}_{\boldsymbol{0}}(i, n, \boldsymbol{J}) \otimes \boldsymbol{h}_m(\boldsymbol{J})], \tag{36}$$

$$\mathbf{S}_\mathrm{e} = (2\pi)^3 \int \mathrm{d}\boldsymbol{J} H_m(\boldsymbol{J}) \mathbf{G}_n^{-1} \cdot [\tilde{\boldsymbol{g}}_{\boldsymbol{0}}(i, j, n, \boldsymbol{J}) \otimes \boldsymbol{h}_m(\boldsymbol{J})]. \tag{37}$$

The constant element matrices $\mathbf{F}_\mathrm{e}$, $\mathbf{U}_\mathrm{e}$ and $\mathbf{S}_\mathrm{e}$ are of the size $N_\mathrm{d} \times M_\mathrm{d}$ and there are $N \times M$ of them.

To compute $\tilde{\boldsymbol{g}}_{\boldsymbol{k}}$, we simply integrate the equations of motion corresponding to the action $\boldsymbol{J}$ or the initial conditions $(\boldsymbol{x}_0, \boldsymbol{v}_0)$ until the particle enters the nth element at time $t_{1,n}$ and exits at $t_{2,n}$. We then calculate the values of the angles at the entry and exit times, $\boldsymbol{w}_{1,n}$ and $\boldsymbol{w}_{2,n} = \boldsymbol{w}_{1,n} + \boldsymbol{\Omega}(t_{2,n} - t_{1,n})$. We then carry out the integrations in (29), (33) and (34) using Gaussian quadrature, typically with 8–15 points. The numerical integration of the equations of motion continues and $\tilde{\boldsymbol{g}}_{\boldsymbol{k}}$ is updated every time that the particle enters element n, until the trajectory closes on itself for periodic orbits or becomes dense in the $\boldsymbol{w}$-space. The only extra effort of this procedure compared to Schwarzschild's method is to perform the integrals over angle variables. In Section 3.3, we show that one can avoid this numerical integration for separable models.

There are additional constraints associated with the *element equations* (31) and (35) at a node shared by several elements, since a physical quantity must have the same value in the Galerkin projections of all those elements. In fact, one can introduce N_t-dimensional column vectors $\boldsymbol{b}, \boldsymbol{c}_i$ and $\boldsymbol{d}_{ij}$ that contain all nodal densities and first- and second-order velocity moments, and because nodes are shared the dimension $N_\mathrm{t} < N \times N_\mathrm{d}$. Similarly, the nodal DFs constitute an M_t-dimensional column vector $\boldsymbol{p}$ where $M_\mathrm{t} < M \times M_\mathrm{d}$ is the total number of distinct nodes in the $\boldsymbol{J}$-space. Equation (31) can thus be written as

$$\boldsymbol{b} = \mathbf{F} \cdot \boldsymbol{p}. \tag{38}$$

This matrix equation can be solved to yield the DF, as parametrized by its nodal values $\boldsymbol{p}$. The rank of the matrix $\mathbf{F}$ is generally less than its dimension N_t, and there are additional constraints that the DF should be non-negative, so in either Schwarzschild's method or the FEM the solution must be sought by linear or quadratic programming (QP) or some other optimization method (see Section 3.4).

Once the solution is known, the nodal values of the streaming velocity and velocity-dispersion tensor are obtained from equations (35), which can be written as

$$\boldsymbol{c}_i = \mathbf{U}(i) \cdot \boldsymbol{p}, \quad \boldsymbol{d}_{ij} = \mathbf{S}(i, j) \cdot \boldsymbol{p}. \tag{39}$$

The $N_\mathrm{t} \times M_\mathrm{t}$ constant global matrices $\mathbf{F}$, $\mathbf{U}$ and $\mathbf{S}$ are generally dense.

Assembling the element equations is the most important step in finite element analysis, and we explain this step for equation (38). Based on the generated FEM mesh, we first determine N_t and M_t (counting only once nodes shared by several elements), allocate the $N_\mathrm{t} \times M_\mathrm{t}$ dimensional matrix $\mathbf{F}$ and initialize it to zero. Within a nested loop over n and m, the labels of the elements in configuration and action space, the matrices $\mathbf{F}_\mathrm{e}(n, m)$ are then computed and inserted in the global matrix $\mathbf{F}$ through the following algorithm: we find the location of $\rho_{i,n}$ in $\boldsymbol{b}$, and the location of $f_{j,m}$ in $\boldsymbol{p}$, and denote them by $I(i, n)$ and $J(j, m)$, respectively. These integer numbers depend on the global numbering of nodes. We then add $\mathbf{F}_\mathrm{e}(n, m)$ to $\mathbf{F}$ using

$$F_{IJ} = F_{IJ} + F_{ij,\mathrm{e}}(n, m), \tag{40}$$

where F_{IJ} and $F_{ij,\mathrm{e}}$ are, respectively, the elements of $\mathbf{F}$ and $\mathbf{F}_\mathrm{e}(n, m)$. The element F_{IJ} in the global matrix will be incremented more than once if the pair (I, J) denotes a node that is shared between neighbouring finite elements. As the matrix $\mathbf{F}$ is assembled, $\boldsymbol{b}$ is also altered and its components b_i $(1 \le i \le N_\mathrm{t})$ are eventually multiplied by $n_s(i)$, which is the number of spatial bins that share the ith node. After assembling $\mathbf{F}$, we thus divide its ith row by $n_s(i)$ and transform $\boldsymbol{b}$ to its original form. This procedure is applied to all systems of element equations that we derive in this study.

3.2 Continuity and Jeans equations

The accuracy of FEM models of equilibrium stellar systems can be improved by adding additional constraints that ensure that the continuity and Jeans equations (10) and (11) are satisfied. Inside the nth element, these equations can be written as

$$H_n(\boldsymbol{x}) \sum_{j=1}^{3} \frac{\partial \boldsymbol{g}_n}{\partial x_j} \cdot \boldsymbol{c}_n^j = 0, \tag{41}$$

$$H_n(\boldsymbol{x}) \sum_{j=1}^{3} \frac{\partial \boldsymbol{g}_n}{\partial x_j} \cdot \boldsymbol{d}_n^{ij} = -H_n(\boldsymbol{x}) \frac{\partial \Phi}{\partial x_i} \boldsymbol{g}_n \cdot \boldsymbol{b}_n, \quad i = 1, 2, 3. \tag{42}$$

Defining

$$\mathbf{T}_n^j = \int H_n(\boldsymbol{x}) \left[\boldsymbol{g}_n \otimes \frac{\partial \boldsymbol{g}_n}{\partial x_j} \right] \mathrm{d}\boldsymbol{x}, \tag{43}$$

$$\mathbf{V}_n(i) = -\int H_n(\boldsymbol{x}) \frac{\partial \Phi}{\partial x_i} [\boldsymbol{g}_n \otimes \boldsymbol{g}_n] \mathrm{d}\boldsymbol{x}, \tag{44}$$

one obtains the Galerkin projections of (41) and (42) as

$$\sum_{j=1}^{3} \mathbf{T}_n^j \cdot \boldsymbol{c}_n^j = 0, \quad \sum_{j=1}^{3} [\mathbf{V}_n(i)]^{-1} \cdot \mathbf{T}_n^j \cdot \boldsymbol{d}_n^{ij} = \boldsymbol{b}_n. \tag{45}$$

We assemble these element equations to obtain the global forms

$$\sum_{j=1}^{3} \mathbf{A}(j) \cdot \boldsymbol{c}_j = 0, \quad \sum_{j=1}^{3} \mathbf{B}(j) \cdot \boldsymbol{d}_{ij} = \boldsymbol{b}. \tag{46}$$

Combining (39) and (46) leads to

$$\sum_{j=1}^{3} [\mathbf{A}(j) \cdot \mathbf{U}(j)] \cdot \boldsymbol{p} = 0, \quad \sum_{j=1}^{3} [\mathbf{B}(j) \cdot \mathbf{S}(i, j)] \cdot \boldsymbol{p} = \boldsymbol{b}. \tag{47}$$

The global matrices $\mathbf{A}$ and $\mathbf{B}$ are assembled, respectively, from the blocks $\mathbf{T}_n^j$ and $[\mathbf{V}_n(i)]^{-1} \cdot \mathbf{T}_n^j$. We make some remarks. (i) The solutions of the continuity and Jeans equations, whether the continuous versions (10) and (11) or their FEM counterparts (46) above, are generally not unique. A notable exception is triaxial potentials of Stäckel form, in which the second-order tensor $\tau^{ij}(\boldsymbol{x})$ is diagonal in ellipsoidal coordinates (van de Ven et al. 2003). (ii) When using C_0 finite elements, as we do here, the moments ρ, u^i and τ^{ij} (equations 7–9) are continuous across element boundaries but generally their derivatives are not; however, since the right-hand sides of the continuity and Jeans equations *are* continuous across boundaries, the combinations of derivatives of u^i and τ^{ij} that appear on the left-hand sides of these equations must also be continuous. (iii) Equations (47) do not say that the mass and momentum flow into each element, through its boundaries, exactly balance their outflows (although the balance will become more and more accurate as the number of nodes increases). Only finite volume methods (LeVeque 2002) and conservative FEMs ensure the exact conservation of physical fluxes and this paper does not discuss those techniques.

The interpolation functions $\boldsymbol{g}_n(\boldsymbol{x})$ used in equations (16) and (17) are identical, that is, we have chosen to use the same interpolation functions for the density and the velocity moments. The results of Section 6 show that this choice works reasonably well. None the less, it is possible, and perhaps desirable, to apply different interpolation functions to model u^i and τ^{ij}, and to use this additional flexibility to improve the accuracy of FEM models constrained by the continuity and Jeans equations. The reason is that the derivatives of streaming velocity and stress components which appear in these equations are naturally less accurate than the density. Therefore, to satisfy the constraints in (38) and (47) with comparable error levels, one could usefully adopt higher order interpolation functions, or use C_1 finite elements to approximate the first- and second-order velocity moments. We have not yet explored this refinement.

3.3 Separable models

The computation of the element matrices $\mathbf{F}_\mathrm{e}$, $\mathbf{U}_\mathrm{e}$ and $\mathbf{S}_\mathrm{e}$ is accelerated when the Hamilton–Jacobi equation is separable for the potential $\Phi(\boldsymbol{x})$. In such a circumstance, the velocity vector can be expressed as $\boldsymbol{v}(\boldsymbol{x}, \boldsymbol{J})$, which implies

$$\mathrm{d}\boldsymbol{v} = \mathcal{Q}(\boldsymbol{x}, \boldsymbol{J}) \mathrm{d}\boldsymbol{J}, \quad \mathcal{Q}(\boldsymbol{x}, \boldsymbol{J}) = \frac{\partial(v_1, v_2, v_3)}{\partial(J_1, J_2, J_3)}. \tag{48}$$

This allows us to bypass the costly integration of orbit equations needed for calculating the Fourier coefficients $\tilde{\boldsymbol{g}}_{\boldsymbol{0}}$. Using (48), we replace the phase-space element $\mathrm{d}\boldsymbol{x}\mathrm{d}\boldsymbol{v}$ by $\mathrm{d}\boldsymbol{x}\mathrm{d}\boldsymbol{J}$ and compute the element matrices from

$$\mathbf{F}_\mathrm{e} = \iint \mathbf{P}(\boldsymbol{x}, \boldsymbol{J}) \mathrm{d}\boldsymbol{x}\mathrm{d}\boldsymbol{J}, \tag{49}$$

$$\mathbf{U}_\mathrm{e} = \iint v_i(\boldsymbol{x}, \boldsymbol{J}) \mathbf{P}(\boldsymbol{x}, \boldsymbol{J}) \mathrm{d}\boldsymbol{x}\mathrm{d}\boldsymbol{J}, \tag{50}$$

$$\mathbf{S}_\mathrm{e} = \iint v_i(\boldsymbol{x}, \boldsymbol{J}) v_j(\boldsymbol{x}, \boldsymbol{J}) \mathbf{P}(\boldsymbol{x}, \boldsymbol{J}) \mathrm{d}\boldsymbol{x}\mathrm{d}\boldsymbol{J}, \tag{51}$$

where

$$\mathbf{P}(\boldsymbol{x}, \boldsymbol{J}) = H_n(\boldsymbol{x}) H_m(\boldsymbol{J}) \mathcal{Q}(\boldsymbol{x}, \boldsymbol{J}) \mathbf{G}_n^{-1} \cdot [\boldsymbol{g}_n(\boldsymbol{x}) \otimes \boldsymbol{h}_m(\boldsymbol{J})]. \tag{52}$$

The integrals over the $\boldsymbol{x}$ and $\boldsymbol{J}$ subdomains can be evaluated using Gaussian quadratures.

In separable models the turning points of orbits and their shapes in the configuration space are known. Therefore, the null integrals in the element matrices can be avoided, and the computational effort is reduced, by a priori identification of the $\boldsymbol{J}$-subspaces whose orbits never enter a selected element in the $\boldsymbol{x}$-space. In fact, the information related to the passage of an orbit through a given element is carried by the function $H_m(\boldsymbol{J})H_n(\boldsymbol{x})$, and before evaluating the integrals we can exclude all (m, n) pairs that give $H_m(\boldsymbol{J})H_n(\boldsymbol{x}) = 0$. For separable models in non-Cartesian coordinates, the velocity components in the Jacobian $\mathcal{Q}$ are replaced by generalized momenta, and the matrix $\mathbf{P}$ is divided by the product of metric coefficients.

3.4 Linear and quadratic programming

The size of the unknown vector $\boldsymbol{p}$ is not necessarily, or usually, equal to the total number of constraints. Even if it were, the solution vector would not necessarily fulfil the requirement that the DF must be non-negative. We therefore employ either linear programming (LP) or QP (Gill, Murray & Wright 1981) and search for p_l, the components of $\boldsymbol{p}$, by minimizing the objective function

$$\mathcal{J} = \sum_{l=1}^{M_\mathrm{t}} C_l p_l + \frac{1}{2}\sum_{l=1}^{M_\mathrm{t}}\sum_{l'=1}^{M_\mathrm{t}} W_{ll'} p_l p_{l'}, \tag{53}$$

with $W_{ll'} = 0$ for LP. The minimization is subject to the inequalities $p_l \geq 0$ (for $l = 1, 2, \ldots, M_\mathrm{t}$) and the equality constraints (38). If we also demand satisfaction of the continuity and Jeans equation these are supplemented by the equality constraints (47). The QP routines begin from a vector $\boldsymbol{p}_0$ that satisfies the imposed constraints with a tolerance of ϵ_f, then proceed to minimize $\mathcal{J}$. The vector $\boldsymbol{p}_0$ is usually called a feasible solution and ϵ_f is the feasibility tolerance; the latter must be greater than the computational accuracy of the variables involved in the constraints.

The weights $W_{ll'}$ are chosen based on the desired attributes of the model, such as bias towards radial or tangential orbits, maximization of a quadratic entropy, or fitting to specified data. For example, if a series of observables o_α are linear functions of the DF,

$$o_\alpha = \sum_{l=1}^{M_\mathrm{t}} O_{\alpha l} p_l, \quad \alpha = 1, \ldots, K, \tag{54}$$

and they are observed to have values $\overline{o}_\alpha$ with observational errors σ_α, then a suitable objective function is specified by

$$C_l = -\sum_{\alpha=1}^{K} \frac{\overline{o}_\alpha O_{\alpha l}}{\sigma_\alpha^2}, \quad W_{ll'} = \sum_{\alpha=1}^{K} \frac{O_{\alpha l} O_{\alpha l'}}{\sigma_\alpha^2}. \tag{55}$$

The LP and QP algorithms we have used can stall at weak local minima or 'dead points'. Whenever this happens, we perturb the solution and restart the algorithm.

4 DERIVATION OF SCHWARZSCHILD'S METHOD

It is now straightforward to show that Schwarzschild's orbit superposition method is a subclass of FEM. We assume for simplicity that the potential is integrable so the orbits are regular. The orbit library in Schwarzschild's method is collected by sampling over the space of initial conditions. For regular orbits there is a one to one and invertible map between $(\boldsymbol{x}_0, \boldsymbol{v}_0)$ and $[\boldsymbol{w}(0), \boldsymbol{J}]$, and Schwarzschild's DFs will have the following form (Vandervoort 1984)

$$f(\boldsymbol{J}) = \frac{\mathcal{M}}{(2\pi)^3}\sum_{m=1}^{M} p_m \delta(\boldsymbol{J} - \boldsymbol{J}_m), \tag{56}$$

where $\delta(\cdots)$ is the Dirac delta function and p_m is the discrete DF associated with an orbit of the action vector $\boldsymbol{J}_m$. Equation (56) is derived from (18) by shrinking the elements in the action space to zero size. The total mass of the galaxy is computed from

$$\mathcal{M} = \iint f(\boldsymbol{J})\mathrm{d}\boldsymbol{J}\mathrm{d}\boldsymbol{w}, \tag{57}$$

which is combined with (56) to obtain the constraint

$$\sum_{m=1}^{M} p_m = 1. \tag{58}$$

Schwarzschild assumes a uniform density ρ_n inside the nth element in configuration space. This implies that there is one node per element ($N_\mathrm{d} = 1$) and that the vector function $\boldsymbol{g}_n(\boldsymbol{x})$ reduces to a scalar constant, $g_n = 1$. Equation (12) then reduces to

$$\rho(\boldsymbol{x}) = \sum_{n=1}^{N} H_n(\boldsymbol{x})\rho_n. \tag{59}$$

The matrix $\mathbf{G}_n$ is now a single number V_n, which is the volume of the nth element. The quantity $\mathcal{M}_n = \mathbf{G}_n \cdot \boldsymbol{b}_n = V_n\rho_n$ will thus be the mass inside the nth element. We substitute (56) and (59) into (31) and obtain

$$\mathcal{M}_n = \mathcal{M}\sum_{m=1}^{M} p_m \tilde{g}_{\boldsymbol{0}}(n, \boldsymbol{J}_m), \tag{60}$$

with the zeroth-order Fourier coefficient given by

$$\tilde{g}_{\boldsymbol{0}}(n, \boldsymbol{J}_m) = \frac{1}{(2\pi)^3}\int H_n[\boldsymbol{x}(\boldsymbol{w}, \boldsymbol{J}_m)]\mathrm{d}\boldsymbol{w}. \tag{61}$$

According to time averages theorem (Binney & Tremaine 2008), the quantity on the right-hand side of (61) is the fraction of time $t_n(\boldsymbol{J}_m)$ that an orbit of action $\boldsymbol{J}_m$ spends in the nth spatial element. Consequently, we obtain

$$\mathcal{M}_n = \mathcal{M}\sum_{m=1}^{M} t_n(\boldsymbol{J}_m)p_m, \tag{62}$$

which is Schwarzschild's equation.

The approach described in Section 3.2 to incorporate constraints based on the continuity and Jeans equations into FEM models does not work for Schwarzschild's method: because the interpolating functions $\boldsymbol{g}_n$ are constants, the matrices $\mathbf{T}_n^j$ defined in equation (43) are zero so the first of equations (45) is trivially satisfied and the second has no solution. Physically, the stress tensor τ_n^{ij} is constant within an element so there is no divergence in the momentum flux to balance the gravitational force per unit volume $-\rho\partial\Phi/\partial x_i$.

The failure of Schwarzschild's method to satisfy the Jeans equations within an element does not imply that the method is incorrect. Indeed, the method *must* satisfy the Jeans equations on larger scales because the assumed discrete DF (56) depends only on the actions and hence must satisfy the CBE, and the Jeans equations are moments of the CBE. The correct statement is that Schwarzschild's method satisfies the Jeans equations approximately if we calculate gradients of the stress tensor *between* adjacent elements and match their sum to $-\rho\nabla\Phi$ at the centre of an element. In this process, which we carry out for spherical systems in Section 5, one must appropriately handle partial derivatives because elements in the configuration space are not usually separated uniformly.

5 SPHERICALLY SYMMETRIC SYSTEMS

In spherical systems, one can use simple shell elements (ring elements for axisymmetric discs). Moreover, the distance of particles from the centre is represented as the Fourier series of the radial angle w_r only. This remarkably simplifies the calculation of the vectorial function $\tilde{\boldsymbol{g}}_{\boldsymbol{0}}$ should one decide to compute the element matrices from (32), (36) and (37). Consider the spherical polar coordinates (r, θ, ϕ) and the corresponding velocities (v_r, v_θ, v_ϕ) where r is the radial distance from the centre, θ is the co-latitude and ϕ is the azimuthal angle. The density of a spherical system is a function of r, its first-order velocity moment $\langle v_r \rangle$ is zero and the following relations hold for second-order velocity moments:

$$\left\langle v_t^2 \right\rangle = 2\left\langle v_\phi^2 \right\rangle = 2\left\langle v_\theta^2 \right\rangle, \quad \langle v_r v_\phi \rangle = \langle v_r v_\theta \rangle = 0, \tag{63}$$

where $v_t^2 = v_\theta^2 + v_\phi^2 = L^2/r^2$ with L being the magnitude of angular momentum vector. We confine ourselves to models with $\langle v_\phi \rangle = \langle v_\theta \rangle = \langle v_\phi v_\theta \rangle = 0$. The continuity equation (mass conservation) is trivially satisfied for such a system. The elements of the stress tensor are

$$\tau^{rr} = \rho\left\langle v_r^2 \right\rangle, \quad \tau^{tt} = \rho\left\langle v_t^2 \right\rangle, \quad \tau^{\theta\theta} = \rho\left\langle v_\theta^2 \right\rangle, \quad \tau^{\phi\phi} = \rho\left\langle v_\phi^2 \right\rangle, \tag{64}$$

and the Jeans equation in the radial direction reads

$$\frac{\mathrm{d}\tau^{rr}}{\mathrm{d}r} + \frac{1}{r}(2\tau^{rr} - \tau^{tt}) = -\rho\frac{\mathrm{d}\Phi}{\mathrm{d}r}. \tag{65}$$

The other two equations, in the θ- and ϕ-direction, do not provide further information.

We consider a mesh of N concentric shell elements and define the nth element by its inner and outer radii r_n and r_{n+1}, respectively. We then approximate the density and velocity moments as

$$\rho(r) = \sum_{n=1}^{N} H_n(r)\boldsymbol{g}_n(r)\cdot\boldsymbol{b}_n, \tag{66}$$

$$\tau^{rr}(r) = \sum_{n=1}^{N} H_n(r)\boldsymbol{g}_n(r)\cdot\boldsymbol{d}_n^{rr}, \tag{67}$$

$$\tau^{tt}(r) = \sum_{n=1}^{N} H_n(r)\boldsymbol{g}_n(r)\cdot\boldsymbol{d}_n^{tt}. \tag{68}$$

The continuity conditions at the boundaries of adjacent elements are $b_{1,(n+1)} = b_{N_\mathrm{d},n}$, $d^{rr}_{1,(n+1)} = d^{rr}_{N_\mathrm{d},n}$ and $d^{tt}_{1,(n+1)} = d^{tt}_{N_\mathrm{d},n}$. Let us now substitute from equations (66)–(68) into (65) and derive its Galerkin projection as

$$\sum_{m=1}^{M} \mathbf{V}_n^{-1}\cdot\left[\mathbf{T}_n^r\cdot\mathbf{S}_\mathrm{e}^{rr}(n,m) - \mathbf{T}_n^t\cdot\mathbf{S}_\mathrm{e}^{tt}(n,m)\right]\cdot\boldsymbol{p}_m = \boldsymbol{b}_n, \tag{69}$$

for $n = 1, 2, \ldots, N$. The matrices $\mathbf{S}_\mathrm{e}^{rr}$ and $\mathbf{S}_\mathrm{e}^{tt}$ are determined from (51) by replacing $v_i v_j$ with v_r^2 and v_t^2, respectively, and we have

$$\mathbf{T}_n^r = \int H_n(r)\left[\boldsymbol{g}_n\otimes\frac{\mathrm{d}\boldsymbol{g}_n}{\mathrm{d}r}\right]r^2\mathrm{d}r + 2\mathbf{T}_n^t, \tag{70}$$

$$\mathbf{T}_n^t = \int H_n(r)\left[\frac{1}{r}\boldsymbol{g}_n\otimes\boldsymbol{g}_n\right]r^2\mathrm{d}r, \tag{71}$$

$$\mathbf{V}_n = -\int H_n(r)\frac{\mathrm{d}\Phi}{\mathrm{d}r}\left[\boldsymbol{g}_n\otimes\boldsymbol{g}_n\right]r^2\mathrm{d}r. \tag{72}$$

All other equations of Section 3 can be directly applied to spherical systems using the following substitutions:

$$\mathrm{d}\boldsymbol{x} = 4\pi r^2\mathrm{d}r, \quad \mathrm{d}\boldsymbol{v} = \mathcal{Q}(\boldsymbol{x},\boldsymbol{J})\mathrm{d}\boldsymbol{J} = \frac{4\pi L\mathrm{d}E\mathrm{d}L}{r^2 v_r}, \tag{73}$$

where E is the orbital energy of particles:

$$E = \frac{1}{2}v_r^2 + \frac{L^2}{2r^2} + \Phi(r). \tag{74}$$

If we apply the FEM without Jeans equation constraints we must satisfy the linear constraint equations $\boldsymbol{b} = \mathbf{F}\cdot\boldsymbol{p}$ (equation 38). If we include the Jeans equation constraints we assemble equations (69) to a global form $\mathbf{T}\cdot\boldsymbol{p} = \boldsymbol{b}$ and combine this with $\boldsymbol{b} = \mathbf{F}\cdot\boldsymbol{p}$ to give

$$(\mathbf{T} - \mathbf{F})\cdot\boldsymbol{p} = \boldsymbol{0}. \tag{75}$$

In the C_0 finite element formulation, it is difficult to construct a function (here the stress components) and its derivatives with the same accuracy. Therefore, we replace the equality constraints (75) with the weaker inequality constraints

$$0 \le \epsilon_n \le \epsilon_\mathrm{max}, \tag{76}$$

where ϵ_n are the normalized components of the residual vector $(\mathbf{T} - \mathbf{F})\cdot\boldsymbol{p}$, defined as

$$\epsilon_n = \frac{1}{b_n}\sum_{l=1}^{M_\mathrm{t}}(T_{nl} - F_{nl})p_l, \quad n = 1, 2, \ldots, N_\mathrm{t}, \tag{77}$$

and minimize $\mathcal{J}$ by setting

$$C_l = \sum_{n=1}^{N_\mathrm{t}}\frac{T_{nl} - F_{nl}}{b_n}. \tag{78}$$

Here T_{nl} and F_{nl} are the elements of $\mathbf{T}$ and $\mathbf{F}$, respectively. The value of ϵ_max cannot be arbitrarily small: at large radii the magnitudes of the stresses become comparable to the numerical errors, and the Jeans equations are correspondingly less accurate. In our calculations, we have been able to secure convergence with ϵ_max as small as $\sqrt{\epsilon_f}$ over a wide radial range.

It is worth deriving the weighted residual form of the Jeans equation for discrete Schwarzschild models to investigate whether applying this as a constraint improves the accuracy of these models. For $\boldsymbol{g}_n = 1$, the density and second velocity moments are constant inside each element and the vectors $\boldsymbol{b}_n$, $\boldsymbol{d}_n^{rr}$ and $\boldsymbol{d}_n^{tt}$ in (66)–(68) are replaced by the scalars ρ_n, τ_n^{rr} and τ_n^{tt}, respectively. We rewrite (65) as

$$\frac{1}{r^2}\frac{\mathrm{d}(r^2\tau^{rr})}{\mathrm{d}r} - \frac{\tau^{tt}}{r} = -\rho\frac{\mathrm{d}\Phi}{\mathrm{d}r}. \tag{79}$$

We obtain the Galerkin projection through multiplying the differential equation (79) by $H_n(r)r^2\mathrm{d}r$ and integrating over the nth spatial element. For the first term this procedure gives $F(r_{n+1}) - F(r_n)$ where $F(r) = r^2\tau^{rr}(r)$. Since τ^{rr} is discontinuous at the element boundaries we must make some arbitrary choice; after some experimentation we have found that the best convergence is obtained by taking $\tau^{rr}(r_n)$ to be τ^{rr}_{n-1}, that is, the value of the stress in the element interior to the boundary. Then the discretized Jeans equation is

$$r_n^2\tau^{rr}_{n-1} - r_{n+1}^2\tau_n^{rr} + \frac{r_{n+1}^2 - r_n^2}{2}\tau_n^{tt} = \rho_n\int_{r_n}^{r_{n+1}}\frac{\mathrm{d}\Phi}{\mathrm{d}r}r^2\mathrm{d}r. \tag{80}$$

This difference equation is not necessarily satisfied by an optimization procedure that attempts to fit observables using a DF of the form (56). We note that τ^{rr}_{n-1} and τ_n^{rr} are normal stresses exerted on

the nth shell element at its inner and outer boundaries. For sufficiently thin elements when $(\Delta r_n)^2 \ll r_n \Delta r_n$, one may replace r_{n+1}^2 by $r_n^2 + 2r_n\Delta r_n$ and write (80) as

$$\frac{\tau_{n-1}^{rr} - \tau_n^{rr}}{\Delta r_n} + \frac{1}{r_n}\left[\tau_n^{tt} - 2\tau_n^{rr}\right] = \rho_n \left[\frac{\mathrm{d}\Phi}{\mathrm{d}r}\right]_{r=r_n}, \tag{81}$$

which is the discrete counterpart of (65) obtained using a backward difference scheme.

6 EXAMPLES

We illustrate the performance of FEM for spherically symmetric systems by constructing ergodic and anisotropic DFs for the Hernquist (1990) model. Each orbit is characterized by its maximum and minimum galactocentric distances $r_{\max}(\boldsymbol{J})$ and $r_{\min}(\boldsymbol{J})$. We define

$$a(\boldsymbol{J}) = \frac{r_{\max} + r_{\min}}{2}, \quad e(\boldsymbol{J}) = \frac{r_{\max} - r_{\min}}{r_{\max} + r_{\min}}, \tag{82}$$

and the finite element mesh is generated in (a, e)-space instead of action space.

The potential-density pair for the Hernquist model is given by

$$\Phi(r) = -\frac{1}{1+r}, \quad \rho(r) = \frac{1}{2\pi}\frac{1}{r(1+r)^3}. \tag{83}$$

Since ρ diverges towards the centre, and to resolve the behaviour of functions in the central regions, the nodes of our N shell elements are distributed with equal logarithmic spacing, using the power law

$$r_n = 10^{-\gamma_1 + \alpha_1 y(n,N)},$$
$$y(n, N) = \frac{1}{2(N+1)} + \frac{n-1}{N+1}, \quad n = 1, \ldots, N+1. \tag{84}$$

We use simple double-node elements with $N_\mathrm{d} = 2$ (no interior nodes) and linear interpolating functions in the radial direction,

$$\boldsymbol{g}_n(r) = \left[\frac{1}{2}(1-\bar{r}) \quad \frac{1}{2}(1+\bar{r})\right], \quad \bar{r} = \frac{2(r-r_n)}{r_{n+1}-r_n} - 1. \tag{85}$$

Having the grid information and interpolation functions, the matrices $\mathbf{G}_n$, $\mathbf{T}_n^r$, $\mathbf{T}_n^t$ and $\mathbf{V}_n$ can be calculated.

The mesh in the two-dimensional (a, e)-space consists of $M = M_a \times M_e$ rectangular elements, each with $M_\mathrm{d} = 4$ nodes (Fig. 2). For the mth element sitting in the jth row and ith column of the mesh, the local coordinates (ξ, η) are defined as

$$\xi = \frac{2(a - a_i)}{a_{i+1} - a_i} - 1, \quad i = 1, 2, \ldots, M_a, \tag{86}$$

$$\eta = \frac{2(e - e_j)}{e_{j+1} - e_j} - 1, \quad j = 1, 2, \ldots, M_e, \tag{87}$$

where $m = (i-1) \times M_e + j$ and

$$a_{i'} = 10^{-\gamma_2 + \alpha_2 y(i', M_a)}, \quad e_{j'} = y(j', M_e). \tag{88}$$

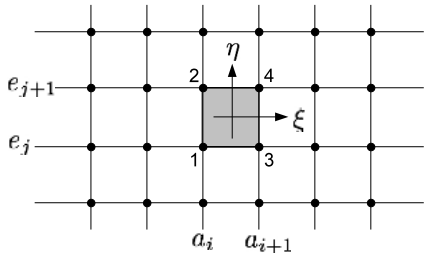

Figure 2. Two-dimensional finite element mesh in the (a, e)-space. Local variables (ξ, η) vary in the interval $[-1, +1]$ and the centre of element is located at $(\xi, \eta) = (0, 0)$.

The minimum eccentricity in our grid is $e_1 = \frac{1}{2}/(M_e + 1)$; we avoid zero-eccentricity orbits because of the singularity of the Jacobian $\mathcal{Q}(\boldsymbol{x}, \boldsymbol{J})$ at the circular orbit boundary of the action space. We do not have exactly radial orbits in our models as the maximum eccentricity in our grid is $e_{M_e+1} = 1 - \frac{1}{2}/(M_e + 1)$.

The four nodal coordinates of each element are given by

$$(\xi_1, \eta_1) = (-1, -1), \quad (\xi_2, \eta_2) = (-1, +1),$$
$$(\xi_3, \eta_3) = (+1, -1), \quad (\xi_4, \eta_4) = (+1, +1). \tag{89}$$

The DF at (ξ_k, η_k) is indexed by k and the following interpolation functions are used inside the mth element

$$h_{j,m}(\xi, \eta) = \frac{1}{4}(1 + \xi_j\xi)(1 + \eta_j\eta), \quad j = 1, 2, 3, 4. \tag{90}$$

These are smooth quadratic functions that behave linearly along element boundaries. DFs at the common nodes of adjacent elements must be equal in order to build a continuous $f(\boldsymbol{J})$. This condition is taken into account in assembling the global matrices $\mathbf{F}$, $\mathbf{U}$ and $\mathbf{S}$. Our experiments show that FEM is not highly sensitive to the parameters γ_i and α_i $(i = 1, 2)$ but they should be chosen so that at least one orbit passes through each element. The cost of computations is remarkably reduced by minimizing the size M of the grid in action space while keeping the number of constraints constant. In such conditions, securing a feasible solution $\boldsymbol{p}_0$ becomes harder though the choices $\gamma_1 = \gamma_2$ and $\alpha_1 = \alpha_2$ are often helpful when the same element nodes are used in the r and a spaces. The reason is that a solution $\boldsymbol{p} = \mathbf{F}^{-1} \cdot \boldsymbol{b}$ always exists in the limit of a DF composed of circular orbits, $f = f_0(a)\delta(e^2)$, and one can imagine smooth DFs of the form

$$f = (1 - \alpha) f_0(a)\delta(e^2) + \alpha f_1(a, e), \quad 0 \le \alpha < 1, \tag{91}$$

which are found by the optimizer through varying α and f_1.

6.1 Ergodic distribution functions

We begin our numerical experiments by constructing ergodic DFs; these give an isotropic stress tensor with

$$2\tau^{rr} = \tau^{tt} \longrightarrow (2\mathbf{S}^{rr} - \mathbf{S}^{tt}) \cdot \boldsymbol{p} = \mathbf{0}. \tag{92}$$

Here $\mathbf{S}^{rr}$ and $\mathbf{S}^{tt}$ are $N_\mathrm{t} \times M_\mathrm{t}$ matrices assembled from $\mathbf{S}_\mathrm{e}^{rr}$ and $\mathbf{S}_\mathrm{e}^{tt}$, respectively. We solve this particular problem by LP. Our first FEM model has $N = 50$ shell elements in the configuration space and a mesh of $M_a \times M_e = 40 \times 40$ elements in the (a, e)-space. The grid points have been obtained by setting $\alpha_1 = \alpha_2 = 3$ and $\gamma_1 = \gamma_2 = 2$. The innermost grid point in the configuration space is at $r_1 = 0.0107$ and the outermost at $r_{N+1} = 9.345$ where the Hernquist model density is 1.54×10^{-5}. The innermost and outermost grid points in the a-direction are located at $a_1 = 0.0109$ and $a_{M_a+1} = 9.1921$. The total number of unknown nodal DFs is $M_\mathrm{t} = 1681$. For N linear elements with $N_\mathrm{d} = 2$ nodes per element, we have $N \times (N_\mathrm{d} - 1) + 1 = 51$ equality constraints to build ρ from $\boldsymbol{b} = \mathbf{F} \cdot \boldsymbol{p}$, and 51 equality constraints to impose the isotropy condition (92). There are also 51 inequalities of the type (76) when the Jeans constraints are present. The weights of all nodal DFs in the objective function $\mathcal{J} = \sum_l C_l p_l$ are assumed to be equal: $C_l = 1$ $(l = 1, 2, \ldots, M_\mathrm{t})$ in the absence of Jeans constraints, which corresponds to minimizing the sum of the values of the DF at all the nodes. Experiments with other choices for the C_l suggest that our solutions are not sensitive to this choice, which is to be expected since the ergodic DF for a spherical system with a given density and potential is unique.

We also construct a model with the parameters $N = 50$, $\alpha_1 = \alpha_2 = 3$ and $\gamma_1 = \gamma_2 = 2$ as in the first model, but with a coarser

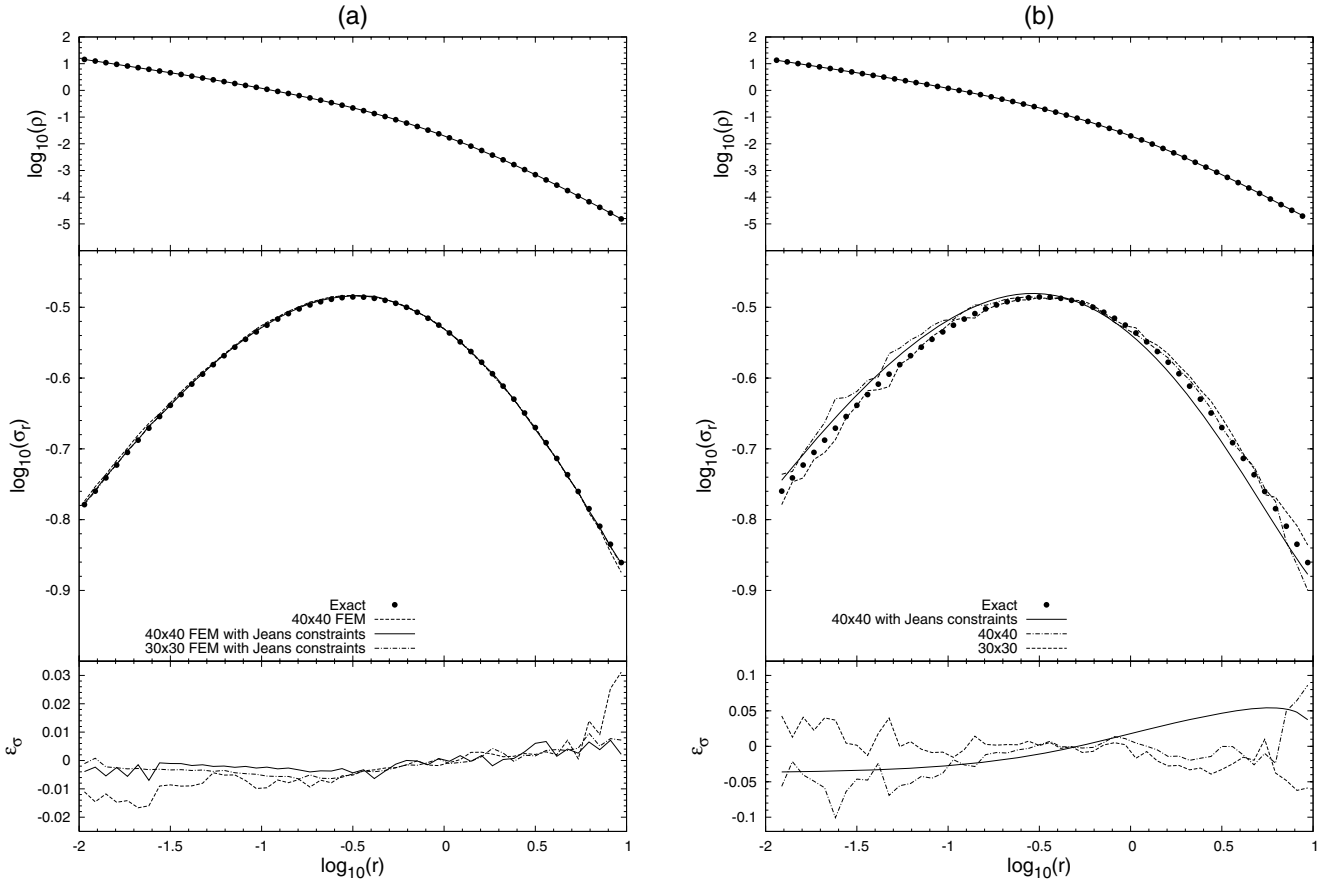

Figure 3. The computed profiles of the density ρ, radial velocity dispersion σ_r and fractional dispersion error ϵ_σ for the Hernquist model with ergodic DF. In all FEM and Schwarzschild experiments, the anisotropy parameter $\beta(r)$ is zero over elements with an accuracy of 10^{-8}. The exact values of ρ and σ_r are shown by filled circles. (a) FEM results for $N = 50$ shells in the configuration space. Three models are shown, although they are indistinguishable in the top panel and almost indistinguishable in the middle panel: $M_a \times M_e = 40 \times 40$ elements in the (a, e)-space, no Jeans equation constraints (dashed line); $M_a \times M_e = 40 \times 40$ with Jeans constraints (solid line), and $M_a \times M_e = 30 \times 30$ with Jeans constraints (dot–dashed line). (b) Schwarzschild models with $N = 50$ shells. The three models are: $M_a \times M_e = 30 \times 30$ elements in (a, e)-space, no Jeans equation constraints (dashed line); $M_a \times M_e = 40 \times 40$, no Jeans constraints (dot–dashed line); $M_a \times M_e = 40 \times 40$ with Jeans constraints (solid line). Note that the vertical scales in the two bottom panels are different.

grid of $M_a \times M_e = 30 \times 30$ in the (a, e)-space. These give $a_1 = 0.0112$, $a_{M_a+1} = 8.9457$ and $M_t = 961$.

In all of our runs with and without Jeans equation constraints, $\rho(r)$ is successfully reconstructed with a fractional error $\leq 10^{-8}$, and the anisotropy parameter $\beta(r) = 1 - \frac{1}{2}\tau^{tt}/\tau^{rr}$ is zero to within the feasibility tolerance $\epsilon_f = 10^{-8}$. The fractional accuracy in satisfying the Jeans equations is controlled by the parameter $\epsilon_{\max}$ (equation 76). We initialize $\epsilon_{\max}$ to $\mathcal{O}(10^{-4})$ for $r < 3.2$ and $\mathcal{O}(10^{-2})$ at larger radii where the magnitude of τ^{rr} becomes comparable with the discretization errors, which are greater than the feasibility tolerance by several orders of magnitude. At some nodes the prescribed $\epsilon_{\max}$ may be too small to allow for a reasonable optimal solution. We tolerate constraint violations of up to 5 per cent at individual nodes should the rms of ϵ_n (over all nodes) be of $\mathcal{O}(10^{-3})$.

Fig. 3(a) displays the computed density $\rho(r)$, radial velocity dispersion $\sigma_r(r)$, and fractional error $\epsilon_\sigma = 1 - \sigma_r/\sigma_r^0$, where the exact dispersion σ_r^0 comes from equation (10) in Hernquist (1990). The FEM solution constrained by equation (92) but not the Jeans equation constraint (75) exhibits an error of 3 per cent in the outermost element, and a systematic drift from $\sigma_r^0(r)$ in the central regions, amounting to a 1.5 per cent error for $r \lesssim 0.03$. If we had not any information about the exact dispersion profile, the computed σ_r was smooth enough to be accepted as a solution. When we add the Jeans equation constraint the mean error is reduced by a factor of 2.5, typically to $\lesssim$0.3 per cent. The errors of up to 0.5 per cent near the inner and outer boundaries are due to FEM discretization and model truncation, and hence are not improved by adding the Jeans equation constraint; these can be suppressed by using boundary elements to cover the currently neglected ranges $[0, r_1)$ and (r_{N+1}, ∞). Adding more spatial elements is not helpful beyond the radius at which the stresses become as small as the discretization errors.

To compare FEM with Schwarzschild's method, we build Schwarzschild models using the same $N = 50$ shells in configuration space, with a discrete DF (equation 56) that is non-zero only at actions $\boldsymbol{J}_m$ given by the nodes of the mesh defined in (88). The equality constraints in the LP routine consist of Schwarzschild's equation (62) and a variant of the isotropy constraints (92). We use the same tolerances as in the FEM models. The profiles of ρ, σ_r and ϵ_σ in our Schwarzschild models are shown in Fig. 3(b) for two grids, $M_a \times M_e = 30 \times 30$ and 40×40. It is seen that the dispersion error ϵ_σ is as large as 10 per cent, about five times larger than in the FEM method; the radial fluctuations in ϵ_σ are also larger. We remark that the model with the smaller orbit library or action-space grid ($M_a \times M_e = 30 \times 30$) is *more* accurate, which highlights the fact that Schwarzschild's method is sensitive to the locations $\boldsymbol{J}_m$

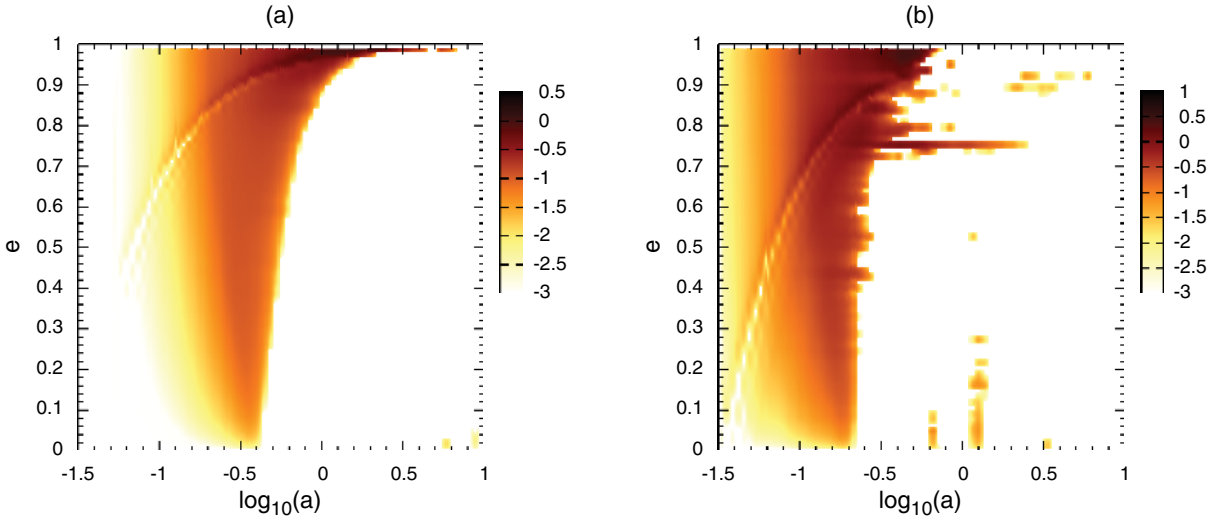

Figure 4. Isocontours of $\log_{10}(f)$ for radially biased models unconstrained (panel a) and constrained (panel b) by the differential Jeans equation (65). Both models have 70×70 elements in the (a, e)-space and 70 shell elements in the configuration space.

of the delta functions in the action space. Special orbit sampling strategies can reduce this sensitivity and enhance the accuracy of computations (Thomas et al. 2004). Note that this sensitivity is not present in FEM; Fig. 3(a) shows FEM models with 30×30 and 40×40 grids and the error is generally smaller with the larger grid, as expected.

Adding the constraints (80) to the optimization procedure brings a dramatic change for Schwarzschild models. For the model with $M_a \times M_e = 40 \times 40$, the curve of σ_r and its fractional error are astonishingly smooth when the Jeans constraints are imposed, although the rms error is not substantially reduced. By following this procedure, the sensitivity to the sampling of orbits (or choosing the location of delta functions) disappears. Our experiments with models constrained by the Jeans equation show that the deviation between the exact and computed curves of σ_r is of $\mathcal{O}(\Delta r_n)$. An exact match is anticipated in the limit of $\Delta r_n \to 0$, but convergence to the correct solution will be slow and costly. In contrast, FEM converges at a rate $\mathcal{O}(h^{p+1})$ where h is the element size (in either action space or configuration space), and p is the order of the interpolating polynomial ($p = 1$ in our case). Thus, FEM should, and does, converge faster than Schwarzschild's method by one order in the element size.

6.2 Anisotropic distribution functions

In this subsection we use FEM and QP optimization to construct anisotropic DFs. We begin with a model constructed without Jeans equation constraints (ϵ_n varies freely) having $N = 70$ spatial shell elements and a mesh $M_a \times M_e = 70 \times 70$ in (a, e)-space. We set $\gamma_1 = \gamma_2 = -1.5$ and $\alpha_1 = \alpha_2 = 2.5$, which correspond to $r_1 = a_1 = 0.0329$ and $r_{N+1} = a_{M_a+1} = 9.6027$. The weights in the objective function (53) are chosen as $C_l = 0$ and

$$W_{ll'}(\boldsymbol{J}) = \delta_{ll'}\Big[1 - e^2(\boldsymbol{J}_l)\Big], \quad l = (i'-1)(M_e+1) + j', \\ i' = 1, 2, \ldots, M_a + 1, \\ j' = 1, 2, \ldots, M_e + 1, \tag{93}$$

which is designed to minimize the population of low-eccentricity orbits. Note that $W_{ll'}$ is positive definite so there is a single global minimum of the objective function. The node l in the (a, e)-space is located at $(a_{i'}, e_{j'})$ where $a_{i'}$ and $e_{j'}$ are computed from (88). We thus have $e(\boldsymbol{J}_l) = e_{j'}$. There are $(M_a + 1) \times (M_e + 1) = 5041$ unknown components of $\boldsymbol{p}$, and 71 equality constraints that correspond to $\boldsymbol{b} = \mathbf{F} \cdot \boldsymbol{p}$. The QP routine converges and finds the global minimum $\mathcal{J} = 3.218$ for the objective function. Fig. 4(a) shows the isocontours of the computed DF. The smoothness of the DF is evident. The narrow curved feature is inherited from a feasible solution: the QP method smooths the distribution around a feasible solution $\boldsymbol{p}_0$ that satisfies problem constraints. Since the number of non-zero components of $\boldsymbol{p}_0$ is much less than M_t, the subdomain covered by that feasible solution in the action space shows up as a distinct feature.

To probe whether the Jeans equation is satisfied in this model, we have calculated the distribution of the errors ϵ_n in the Jeans equation (77), and we display these in Fig. 5. For this model, the rms error,

$$\hat{\epsilon} = \left[\frac{1}{N_t}\sum_{n=1}^{N_t}\epsilon_n^2\right]^{1/2}, \tag{94}$$

is $\hat{\epsilon} = 0.226$. It is evident that the differential Jeans constraints (69) have been violated by a large margin in the innermost element, and this problem bleeds over into the stresses in nearby elements, out to $r \simeq 0.3$.

We now include the differential Jeans equation constraint (75) in the solution procedure. Since the number of constraints has been increased, the QP algorithm yields a larger objective, $\mathcal{J} = 54.607$. We find $\hat{\epsilon} = 0.056$ which is four times smaller than the rms error in the unconstrained model. The relatively large errors in the outermost elements are due to discretization errors, just as in the case of the ergodic solutions of the preceding subsection, and could be corrected by a proper boundary element.

The computed DF (displayed in Fig. 4b) is now less smooth and has developed several narrow eccentricity spikes, the strongest of which is at $e \simeq 0.75$. The centroid of the DF has also shifted to smaller a. The narrow curved feature has also shifted, because the number of constraints has been doubled and a new feasible solution has emerged. There are several isolated small rectangular regions with non-zero f; these would have been delta functions in Schwarzschild's approach, but now occupy subdomains containing at least four elements. The continuity and differentiability of

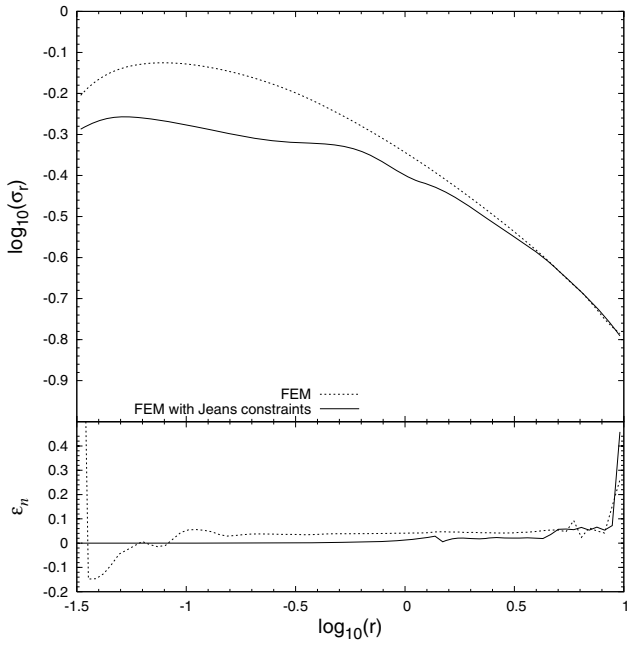

Figure 5. The residuals ϵ_n and radial velocity dispersion $\sigma_r = \langle v_r^2 \rangle^{1/2}$ for models constrained (solid lines) and unconstrained (dotted lines) by the differential Jeans equation (65). The node number n and its corresponding radial distance r_n are related through $\log_{10}(r_n) = -1.5 + 2.5y(n, N)$. The error in the innermost bin is off the scale of the lower panel, $\epsilon_1 = 1.828$. The larger errors in the outermost elements arise because the magnitude of the stress τ^{rr} is comparable to the discretization errors for $r \gtrsim 8$.

f are clear even in such isolated subdomains. The radial velocity dispersions of the two solutions (with and without Jeans equation constraints) are compared in Fig. 5.

Since some wiggles exist in the dispersion σ_r of the constrained model and the magnitude of $\mathcal{J}$ is substantially larger than in the unconstrained model, we suspect that QP has not been able to find a global minimum corresponding to a reasonably smooth DF. This may have occurred because our strict $\epsilon_n \to 0^+$ constraints have shielded the global minimum. To locate the global minimum, one can identify unnecessarily small values of ϵ_n and ease the corresponding constraints that may have strongly constrained $\mathrm{d}\tau^{rr}/\mathrm{d}r$ in a $\boldsymbol{p}$-subspace where this gradient is actually inaccurate due to errors in the computed τ^{rr}. An alternative way of employing Jeans constraints, which gives smoother DFs, is discussed below.

We integrate equation (65) to obtain

$$r^2\tau^{rr} = \int_r^\infty r\tau^{tt}\mathrm{d}r - \int_r^\infty r^2\rho\frac{\mathrm{d}\Phi}{\mathrm{d}r}\mathrm{d}r, \tag{95}$$

in which we have imposed the boundary condition that the stresses vanish at infinity. Substituting from (66)–(68) into (95), and performing integrals over individual elements, gives

$$\sum_{n=1}^{N} H_n(r)r^2\boldsymbol{g}_n\cdot\boldsymbol{d}_n^{rr} = \sum_{n=1}^{N} H_n(r)\left(\boldsymbol{g}_n^{tt}\cdot\boldsymbol{d}_n^{tt} + \boldsymbol{g}_n^{\Phi}\cdot\boldsymbol{b}_n\right), \tag{96}$$

where

$$\boldsymbol{g}_n^{tt}(r) = \int r\boldsymbol{g}_n(r)\mathrm{d}r, \quad \boldsymbol{g}_n^{\Phi}(r) = -\int r^2\frac{\mathrm{d}\Phi}{\mathrm{d}r}\boldsymbol{g}_n(r)\mathrm{d}r.$$

Operating with $\mathrm{d}r\,H_n(r)\boldsymbol{g}_n(r)\otimes$ on (96) and integrating over the r-domain leave us with

$$\sum_{m=1}^{M}\tilde{\mathbf{V}}_n^{-1}\cdot[\mathbf{G}_n\cdot\mathbf{S}_{\mathrm{e}}^{rr}(n,m) - \tilde{\mathbf{T}}_n^{t}\cdot\mathbf{S}_{\mathrm{e}}^{tt}(n,m)]\cdot\boldsymbol{p}_m = \boldsymbol{b}_n \tag{97}$$

for $n = 1, 2, \ldots, N$ with

$$\tilde{\mathbf{V}}_n = \int H_n(r)\boldsymbol{g}_n\otimes\boldsymbol{g}_n^{\Phi}\mathrm{d}r, \quad \tilde{\mathbf{T}}_n^{t} = \int H_n(r)\boldsymbol{g}_n\otimes\boldsymbol{g}_n^{tt}\mathrm{d}r. \tag{98}$$

One can assemble equations (97) into a global form $\tilde{\mathbf{T}}\cdot\boldsymbol{p} = \boldsymbol{b}$ and follow the procedure of Section 5 by replacing $\mathbf{T}$ with $\tilde{\mathbf{T}}$ in equations (75)–(78). The advantage of these *integral Jeans constraints* (97) over their differential counterparts (69) is that they do not involve derivatives of the interpolating functions and τ^{rr}.

We have assumed the same model properties as in Fig. 4 and constructed a smooth DF (top panel in Fig. 6) using the integral Jeans equation. To impose the constraints $\tilde{\mathbf{T}}\cdot\boldsymbol{p} = \boldsymbol{b}$ we have minimized the new residuals

$$\tilde{\epsilon}_n = \frac{1}{b_n}\sum_{l=1}^{M_{\mathrm{t}}}(\tilde{T}_{nl} - F_{nl})p_l, \quad n = 1, 2, \ldots, N_{\mathrm{t}}, \tag{99}$$

using only the lower zero bound on them: $\tilde{\epsilon}_n \geq 0$. Fig. 6 displays $\sigma_r(r)$ and the variation of $\tilde{\epsilon}_n$ for models that are unconstrained and constrained by the integral Jeans equation. The close agreement between the radial dispersion curves of the unconstrained and constrained models shows that the DF of the unconstrained model, which is identical to the model of Fig. 4(a), is accurate and smooth enough to satisfy the integral Jeans equation. For the constrained model, we have found $\mathcal{J} = 3.453$ which is close to the unconstrained minimum $\mathcal{J} = 3.218$, indicating convergence to the global minimum. Smaller values of $\tilde{\epsilon}_n$ in the central regions of the unconstrained model, compared to what we displayed in Fig. 5 for ϵ_n, show that the DF constructed by FEM satisfies the integral Jeans constraints more accurately than differential ones. The correction $\tilde{\epsilon}_n \to 0^+$ in the constrained model yields satisfactory results in the central regions, but again, the outermost element shows a large error because of the model truncation.

We are also able to construct anisotropic models with prescribed anisotropy profiles. In terms of $\beta(r)$, the Jeans equation reads

$$\frac{\mathrm{d}\tau^{rr}}{\mathrm{d}r} + \frac{2\beta(r)}{r}\tau^{rr} = -\rho\frac{\mathrm{d}\Phi}{\mathrm{d}r}. \tag{100}$$

We seek a model with $\beta(r) = -1/(1 + r)$ that has a tangentially biased core and becomes isotropic as $r \to \infty$. For the Hernquist model, this yields the exact solution of equation (100):

$$\tau^{rr} = \rho\sigma_r^2 = \frac{r^2}{2\pi(1+r)^2} \times \left[6\ln\left(\frac{1+r}{r}\right) - \frac{(1+2r)(6r^2+6r-1)}{2r^2(1+r)^2}\right]. \tag{101}$$

We now follow the procedure of Section 5, and project the equation $2(1-\beta)\tau^{rr} = \tau^{tt}$ on the $\boldsymbol{p}$-space. One can verify that

$$\sum_{m=1}^{M}\left[\left(\mathbf{I} - \mathbf{T}_n^{\beta}\right)\cdot\mathbf{S}_{\mathrm{e}}^{rr}(n,m) - \frac{1}{2}\mathbf{S}_{\mathrm{e}}^{tt}(n,m)\right]\cdot\boldsymbol{p}_m = 0 \tag{102}$$

holds for $n = 1, 2, \ldots, N$ where $\mathbf{I}$ is the identity matrix of dimension $N_{\mathrm{d}} \times N_{\mathrm{d}}$ and

$$\mathbf{T}_n^{\beta} = \int H_n(r)\beta(r)\mathbf{G}_n^{-1}\cdot[\boldsymbol{g}_n\otimes\boldsymbol{g}_n]r^2\mathrm{d}r. \tag{103}$$

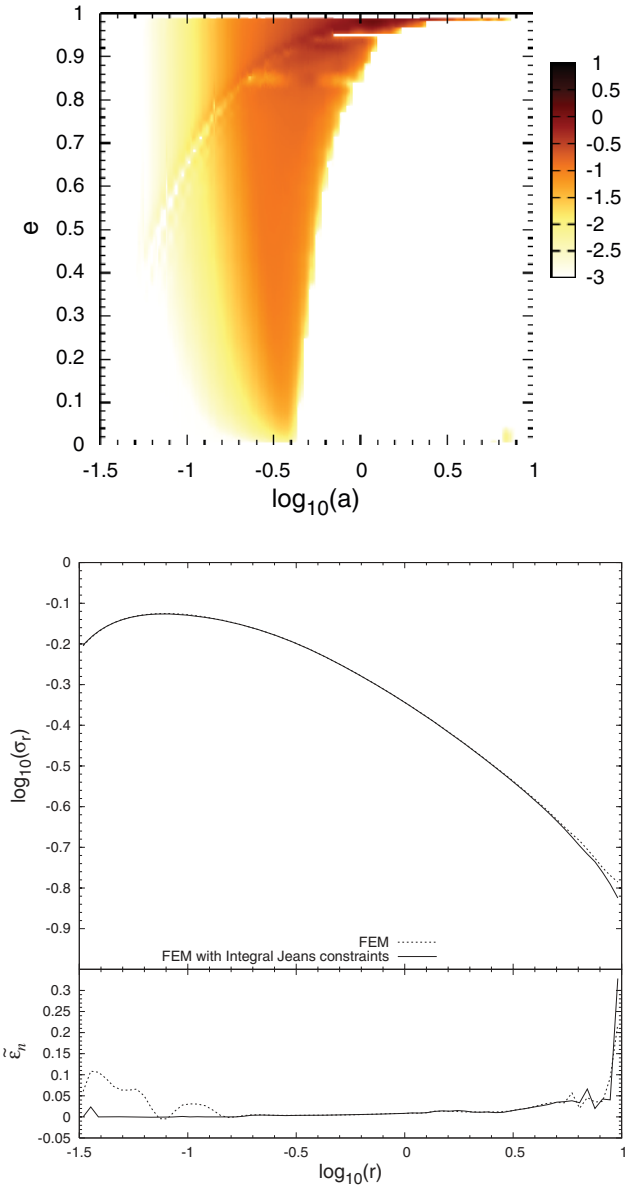

Figure 6. Top: isocontours of $\log_{10}(f)$ for radially biased models constrained by the integral Jeans equation. There are 70×70 elements in the (a, e)-space and 70 shell elements in the configuration space. Bottom: radial velocity dispersion σ_r and the normalized error $\tilde{\epsilon}_n$. The solid and dashed lines correspond to models with and without integral Jeans equation constraints (97), respectively. The DF of the unconstrained model is displayed in Fig. 4(a).

After assembling the system of new constraints (102) into a global form, we ran our FEM code and compared its outcome for σ_r with that of equation (101). Fig. 7 illustrates our results for $N = 50$ spatial shells and $M_a \times M_e = 30 \times 30$ elements in the (a, e)-space. As in the ergodic case, there are distinguishable differences between models constrained and unconstrained by the Jeans equation. We did our calculations using both LP and QP, and could recover theoretical curves of ρ and β with the fractional accuracy 10^{-8} in both approaches. The QP results were not sensitive to the choice of $W_{ll'}$, but we worked with $W_{ll'} = \delta_{ll'} e(\boldsymbol{J}_l)$ $(l = 1, 2, \ldots, M_t)$, which is more consistent with a tangential core. For the LP without Jeans constraints, choosing $C_l = 1$ always gave accurate results. The results of LP and QP were almost identical.

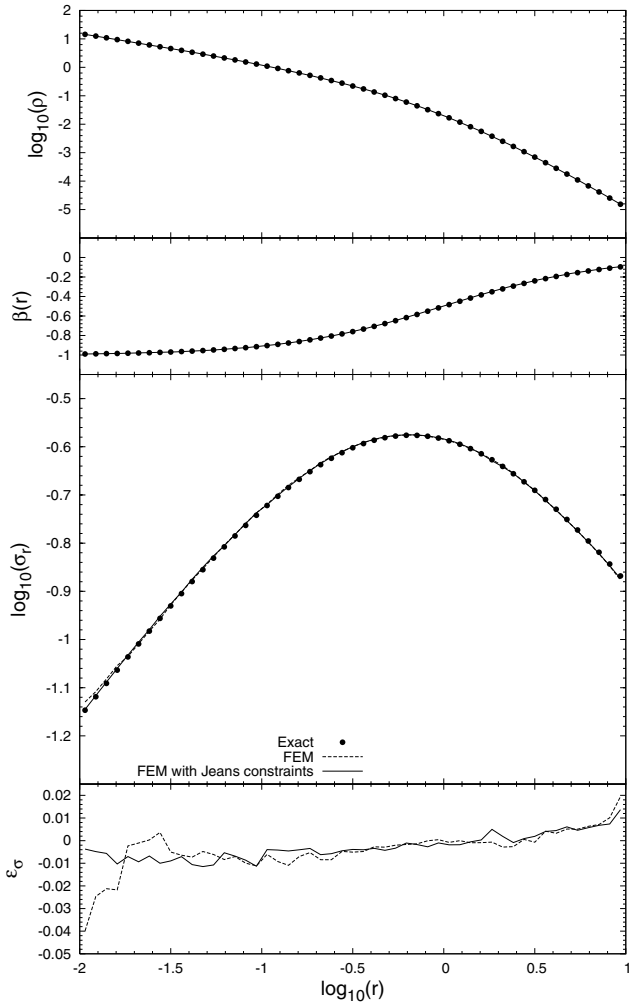

Figure 7. Density, anisotropy parameter, radial velocity dispersion and fractional error ϵ_σ for a model with $\beta(r) = -1/(1 + r)$. The exact values of quantities have been shown by filled circles. The solid and dashed lines correspond to models with and without differential Jeans equation constraints (69), respectively.

7 DISCUSSION

We have demonstrated that Schwarzschild's method for constructing stellar systems can be regarded as a special case of FEM, and that FEM can be used to construct stellar systems that are more accurate approximations to the CBE for given grids in configuration and action space. We have also shown that the accuracy of both Schwarzschild and FEM models can be substantially improved by incorporating the Jeans equations as explicit additional constraints.

There are rigorous mathematical methods for proving the convergence of C_0 FEM schemes to continuous and smooth solutions of initial and boundary value problems described by ordinary and partial differential equations (Szabó & Babuska 1991). Such analyses have also been carried out for eigenvalue problems (Babuska & Rheinboldt 1978) and adaptive FEMs in two-dimensional problems (Morin, Nochetto & Siebert 2002). Although we did not mathematically prove the convergence of FEM-constructed equilibrium DFs, our numerical experiments with the Hernquist model show convergence to the exact values of observables as the element sizes are decreased in a uniform logarithmic mesh. Nevertheless, a major challenge in the convergence analysis of equilibrium models

constructed by FEM is to understand the role of constrained optimization routines and why they appear to give non-unique models in some cases such as given in Fig. 5.

The disadvantage of FEM codes is that they are more time-consuming to write and to run than Schwarzschild codes – but not by a large factor. The main difference is in the procedure where the element matrices are computed and assembled, and in our implementation this procedure contains fewer than twice as many statements. The time required for optimization is the same, since the matrices have the same size in both methods, but the construction of the matrices takes longer in FEM. Overall, the calculations used to produce an FEM model usually take three to five times as long to run as the calculations for the analogous Schwarzschild model.

There are at least two reasons why the higher accuracy provided by FEM is likely to become more important in the future. The first is that the quality of kinematic and photometric observations of galaxies is growing, in particular because of integral-field spectrographs on large telescopes, and higher quality data demand more accurate dynamical models. The second is that the state of the art has gradually progressed from spherical models to axisymmetric and triaxial ones; the higher dimensionality of triaxial models demands much larger grids in configuration space and this in turn calls for numerical methods that converge as a higher power of the characteristic scale of the grid elements.

It is also possible to apply FEM to time-dependent stellar systems, such as barred and spiral galaxies. Since the evaluation of the element integrals does not depend on the nodal variables, the extra computational cost of unsteady problems is associated only with the integration of the evolutionary equations in the time domain. Jalali (2010) has used FEM to study the linear stability of razor-thin disc galaxies and the response of such galaxies to external perturbations such as satellite galaxies.

ACKNOWLEDGMENTS

MAJ thanks the School of Natural Sciences at the Institute for Advanced Study, Princeton, for their generous support. Partial support was also provided by NSF grant AST-0807432 and NASA grant NNX08AH24G. We thank the referee, Peter Vandervoort, for suggestions that substantially improved the paper.

REFERENCES

Babuška I., Rheinboldt W. C., 1978, Int. J. Numer. Meth. Engng., 12, 1597
Binney J., Tremaine S., 2008, Galactic Dynamics, 2nd edn. Princeton Univ. Press, Princeton
Capuzzo-Dolcetta R., Leccese L., Merritt D., Vicari A., 2007, ApJ, 666, 165
Gill P. E., Murray W., Wright M. H., 1981, Practical Optimization. Academic Press, London
Hernquist L., 1990, ApJ, 356, 359
Hunter C., 2002, Space Sci. Rev., 102, 83
Jalali M. A., 2010, MNRAS, 404, 1519
Laskar J., 1990, Icarus, 88, 266
LeVeque R. J., 2002, Finite Volume Methods for Hyperbolic Problems. Cambridge Univ. Press, Cambridge
Morin P., Nochetto R. H., Siebert K. G., 2002, SIAM Rev., 44, 631
Richstone D. O., Tremaine S., 1984, ApJ, 286, 27
Schwarzschild M., 1979, ApJ, 232, 236
Szabó B., Babuška I., 1991, Finite Element Analysis. John Wiley and Sons, New York
Thomas J., Saglia R. P., Bender R., Thomas D., Gebhardt K., Magorrian J., Richstone D., 2004, MNRAS, 353, 391
van den Bosch R. C. E., van de Ven G., Verolme E. K., Cappellari M., de Zeeuw P. T., 2008, MNRAS, 385, 647
Vandervoort P. O., 1984, ApJ, 287, 475
van de Ven G., Hunter C., Verolme E. K., de Zeeuw P. T., 2003, MNRAS, 342, 1056
Zienkiewicz O. C., Taylor R. L., Zhu J. Z., 2005, The Finite Element Method: its Basis and Fundamentals, 6th edn. Elsevier, Butterworth-Heinemann, Oxford

This paper has been typeset from a TEX/LATEX file prepared by the author.